Structural, electronic, vibrational, and thermoelectric properties of Janus Ge$_2$PX(X = N, As, Sb, and Bi) monolayers

Dogukan Hazar Ozbey [1], Mirali Jahangirzadeh Varjovi [1], Gözde Özbal Sargın [1,2]
Hâldun Sevinçli [3,4] and Engin Durgun [1,*]

[1]*UNAM - National Nanotechnology Research Center and Institute of Materials Science
and Nanotechnology, Bilkent University, Ankara 06800, Turkey*
[2]*Sabancı University, Faculty of Engineering and Natural Sciences, 34956 Istanbul, Turkey*
[3]*Department of Materials Science and Engineering, İzmir Institute of Technology, 35430 Urla, İzmir, Turkey*
[4]*Department of Physics, Bilkent University, 06800 Ankara, Turkey*

Two-dimensional (2D) Janus systems have garnered significant scientific interest owing to their novel properties and potential applications. The growing interest in these materials is driven by the idea that their structural asymmetry offers unprecedented opportunities for enhancing thermoelectric performance and unlocking groundbreaking advancements in energy conversion and waste heat utilization. In this context, we present a comprehensive study on the structural, vibrational, electronic, thermal, and thermoelectric properties of Janus Ge$_2$PX(X = N, As, Sb, and Bi) monolayers, using first-principles calculations combined with the Landauer formalism. The suggested configurations exhibit dynamical stability and retain structural integrity even at elevated temperatures. Electronic structure calculations employing hybrid functionals (HSE06) with spin-orbit coupling reveal that Ge$_2$PAs and Ge$_2$PSb monolayers exhibit anisotropic characteristics as indirect semiconductors, while Ge$_2$PN and Ge$_2$PBi exhibit metallic behavior. We also compare the thermal, electronic, and thermoelectric transport properties of these proposed monolayers to binary 2D GeP in the ballistic limit. Notably, both Ge$_2$PAs and Ge$_2$PSb exhibit n-type figure of merit (ZT) values exceeding 1 at 800 K, with their n-type ZT values surpassing that of GeP at room temperature. Our analysis underscores the distinctive structural and electronic properties of Ge$_2$PAs and Ge$_2$PSb monolayers, accompanied by their highly promising thermoelectric performance. These findings position them as strong candidates for energy harvesting and conversion applications.

I. INTRODUCTION

Over the past decade, significant progress has been achieved in exploring and discovering post-graphene two-dimensional (2D) materials, resulting in a vast array of new and exciting structures with unique physical properties [1]. Within the realm of post-graphene monolayers, group IV-V MX compounds (M = Si, Ge, Sn, Pb; X = P, As, Sb, Bi) have emerged as a particularly promising class of 2D materials and become the subject of intense theoretical and experimental investigations [2,3]. Notably, among these compounds, the bulk counterparts of SiP, SiAs, GeP, and GeAs materials have been known to crystallize in the low-symmetric, layered form [4–6], which are stacked by a weak van der Waals (vdW) interaction that considered to be a crucial prerequisite for mechanical exfoliation of 2D materials. Within Ge-based group IV-V materials, the synthesis of binary GeAs and GeP (C2/m group symmetry) has been achieved through micromechanical and liquid phase exfoliation techniques [7]. In addition to the mentioned low-symmetric configuration, studies have reported the existence of a high-symmetric phase (belonging to the $P\bar{6}m2$ space group) for SiP, SiAs, GeP, and GeAs monolayers. This high-symmetric phase has been shown to differ in stability and fundamental properties compared to the low-symmetric configurations and can be synthesized through deposition and self-assembly techniques [2]. These materials' distinctive electronic, optical, and mechanical properties render them highly desirable for a diverse array of potential applications. Group IV-V semiconducting monolayers, for instance, have a strain-induced tunable electron mobility property that can be exploited in future electromechanical devices [8]. Another investigation on the ballistic transport properties of 2D SiP showed that the monolayer is available to be utilized as a channel material in the next-generation field-effect transistors (FETs) [9]. Furthermore, it has been predicted that applying isotropic stretching can effectively convert GeAs monolayer into a direct-gap material, and strained 2D GeAs could be beneficial for n-type semiconductor devices due to enhanced electron mobility [10]. Moreover, the same study has suggested that the diffusion of Li atoms is approximately 1000 times faster on GeP surface than on graphene [10]. A recent theoretical study has also indicated that the Ge$_2$Y$_2$(Y = N, P, As, and Sb) monolayers have great potential for high-performance and room-temperature thermoelectric devices [11]. Efforts to fabricate other 2D Ge-based pnictides are ongoing, driven by experimental endeavors.

*Contact author: durgun@unam.bilkent.edu.tr

Following the advancements in binary monolayers, researchers have increasingly focused on ternary Janus monolayers. These materials have gained prominence due to their diverse array of properties and their potential to facilitate the design of novel devices [12–14]. The breaking of out-of-plane symmetry by combining different elements on each side of the material, Janus monolayers offer a broad range of chemical compositions and electronic characteristics that surpass those attainable with binary systems [15]. The synthesis of Janus MoSSe monolayer and its intrinsic vertical piezoelectric response [16,17] highlighted the significant potential of ternary Janus structures. These exceptional advancements have been followed by the realization of other ternary transition metal dichalcogenides (TMDs), such as WSSe [18,19], PtSSe [20], and their heterostructures [18]. Theoretical studies have further broadened the possibilities beyond TMDs, predicting additional Janus material classes to facilitate the development of novel monolayers. These systems hold great promise for advanced applications across diverse fields, including electronics, optoelectronics [21–23], and photocatalysis [24–27].

Janus derivatives of high-symmetric group IV-V binary monolayers have also been revealed to show intriguing properties. For instance, mirror symmetry breaking in these materials can result in spin-related properties, as it has been reported for 2D PA_2As (A = Si, Ge, Sn, and Pb) structures to exhibit the Stoner ferromagnetic transition upon injection of a hole [28]. Additionally, Rashba-type spin splitting has been discovered in Janus Si_2XY (X, Y = P, As, Sb, and Bi) monolayers, which can be improved by strain and has the potential for spintronic applications [29]. Moreover, X_2PAs (X = Si, Ge, and Sn) systems have been found to possess piezoelectric effect along both in-plane and out-of-plane directions, originating from their asymmetry in both atomic and electronic structures [30]. In light of these theoretical and experimental findings and taking into account the distinctive characteristics of Ge-based group IV-V systems, we present a study where Janus Ge_2PX (X = N, As, Sb, and Bi) monolayers are designed, and their structural, electronic, vibrational, transport, and thermoelectric (TE) properties are uncovered. Initially, we obtain the ground-state arrangement of Janus Ge_2PX monolayers and investigate their dynamical and thermal stability. After verifying the stability of these systems, we examine their vibrational characteristics by conducting a detailed analysis of phonon modes through Raman spectroscopy. Upon elucidating the electronic properties, our investigation shifts towards the examination of electronic transport and TE properties of semiconducting systems in the ballistic regime using the Landauer approach.

II. METHODS

All computational simulations presented in this paper were performed with the Vienna *ab initio* simulation package (VASP) [31–34] in the framework of density functional theory (DFT) [35,36]. The Perdew–Burke–Ernzerhof (PBE) functionals, which employ a generalized gradient approximation (GGA) [37], were utilized to approximate the exchange-correlation potential. The ion-electron interactions were taken into account by using the projected augmented wave method (PAW) [38,39] with a plane-wave cutoff energy of 530 eV. The

sampling of the Brillouin zone (BZ) was achieved through a Monkhorst-Pack scheme [40], using a Γ-centered k-point mesh of $16 \times 16 \times 1$. To prevent spurious interactions, vacuum spacing was chosen to be at least 15 Å along the out-of-plane direction. The vdW interactions were described using the DFT-D3 method with Becke-Johnson damping function [41,42]. The lattice parameters and atomic positions were relaxed until the Hellman-Feynman forces were less than 0.01 eV/Å on each atom. The energy difference between two consecutive electronic and ionic steps was set to 10^{-5} eV and 10^{-4} eV, respectively. To overcome the underestimated band gap (E_g) limitation by GGA-PBE formalism, we employed the Heyd-Scuseria-Ernzerhof (HSE06) hybrid functional approach [43,44], which provides more accurate E_g values. The effect of spin-orbit coupling (SOC) was taken into account for both PBE and HSE06 levels. The phonon band dispersions were investigated by the small displacement method as performed in the PHONOPY package [45], using a $4 \times 4 \times 1$ supercell. The Raman activity of each vibrational mode was calculated via deriving the macroscopic dielectric tensor at Γ point utilizing the small difference technique. Based on the results of the Raman calculations, Raman spectra were obtained by implementing a suitable Gaussian broadening. The thermal stability of the examined systems was analyzed using *ab initio* molecular dynamic (AIMD) simulations at constant temperatures (300 K and 600 K), with time steps of 1 fs and a simulation time of 3 ps. TE coefficients were obtained starting from expressions of the electrical (I_e) and electrical part of the thermal current (I_{th}) based on Landauer formalism

$$I_e = \frac{2e}{h} \int \tau(E)(f_L(E) - f_R(E))dE, \quad (1)$$

$$I_{th} = \frac{2}{h} \int (E - \mu)\tau(E)(f_L(E) - f_R(E))dE, \quad (2)$$

where $f_{L/R} = 1/(1 + e^{\beta_{L/R}(E-\mu_{L/R})})$ are the Fermi distribution (FD) function of left and right reservoirs with $\beta = 1/k_B T_{L/R}$ and $\tau(E)$ is the electronic transmission. In the ballistic limit, $\tau(E)$ equals the number of available channels contributing to the transport at a given energy. The electronic transmission spectrum was calculated by profiting from the knowledge of the electronic band structure with HSE06 functional. It is worth mentioning that high k-point sampling is required to obtain accurate and smooth $\tau(E)$; therefore, $100 \times 100 \times 1$ k-point meshes were used in calculating $\tau(E)$. In the limit of a small temperature difference and bias voltage, $f_L(E) - f_R(E) = (\frac{\partial f_0}{\partial E})e\Delta V - (-\frac{\partial f_0}{\partial E})(\frac{E-\mu}{T})\Delta T$ was obtained by using Taylor expansion [46]. Here, $(-\frac{\partial f_0}{\partial E})$ can be expressed as the Fermi window function, and its width is proportional to $k_B T$. TE transport coefficients, namely, electrical conductance $G_e = e^2 L_0$, Seebeck coefficient (thermopower) $S = (L_1/L_0)/eT$, and electrical thermal conductance $\kappa_{el} = (L_2 - L_1^2/L_0)/T$ can be expressed and straightforwardly derived in terms of orders of L_n integrals [47] where

$$L_n(\mu, T) = -\frac{2}{h} \int \tau(E)(E - \mu)^n \left(-\frac{\partial f_0}{\partial E}\right)dE. \quad (3)$$

The power factor $PF = S^2 G_e$ was obtained with the help of electronic TE coefficients. Similarly, Landauer formalism was conducted to obtain phonon thermal conductance (κ_{ph}), which
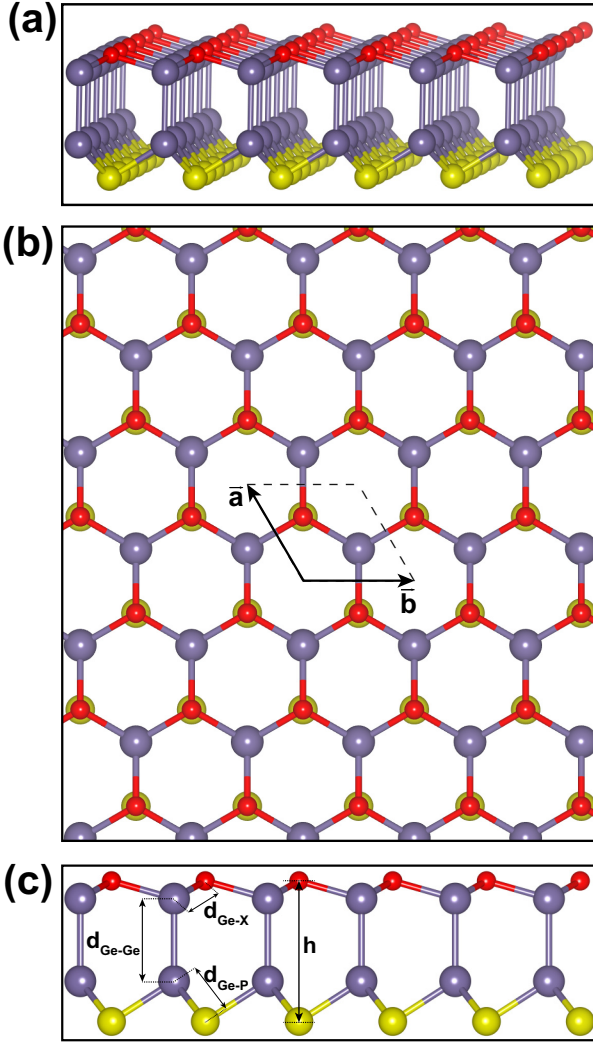
FIG. 1. (a) Side and (b) top views of Janus Ge_2PX monolayer. The unit cell is marked by a dashed-black parallelogram. (c) Bond lengths are denoted for Ge-X, Ge-Ge, and Ge-P bonds. Layer thickness is given with h. X (N, As, Sb, and Bi), germanium, and phosphorus atoms are presented as red, purple, and yellow spheres, respectively.

is expressed as

$$\kappa_{ph} = \frac{1}{2\pi} \int \tau_{ph}(\omega)\hbar\omega \left(\frac{\partial f_{BE}(\omega, T)}{\partial T} \right) d\omega. \qquad (4)$$

Here, $\tau(\omega)$ is the phonon transmission spectrum per width computed using a $200 \times 200 \times 1$ dense q-point sampling. Thermoelectric figure of merit $ZT = S^2 G_e T / (\kappa_{el} + \kappa_{ph})$ can be predicted after obtaining electronic and phonon thermal transport parameters.

III. RESULTS AND DISCUSSION

A. Structure

The crystal structure of Janus Ge_2PX (X = N, As, Sb, and Bi) monolayers, as schematically illustrated in Figs. 1(a) and 1(b), is generated from the binary GeP monolayer. The design involves the substitution of the top-layer P atoms with

TABLE I. Calculated lattice parameter (a), bond lengths for Ge-X, Ge-Ge, and Ge-P bonds ($d_{\text{Ge-}X}$, $d_{\text{Ge-Ge}}$, and $d_{\text{Ge-P}}$), layer thickness (h), electronic band gap energy with PBE functional (E_g^{PBE}), with hybrid functional (E_g^{HSE}), with PBE functional and SOC ($E_g^{\text{PBE-SOC}}$), with hybrid functional and SOC ($E_g^{\text{HSE-SOC}}$). M indicates that the system is metallic.

	a (Å)	$d_{\text{Ge-}X}$ (Å)	$d_{\text{Ge-Ge}}$ (Å)	$d_{\text{Ge-P}}$ (Å)	h (Å)	E_g^{PBE} (eV)	E_g^{HSE} (eV)	$E_g^{\text{PBE-SOC}}$ (eV)	$E_g^{\text{HSE-SOC}}$ (eV)
Ge_2PN	3.32	1.99	2.52	2.28	4.29	M	M	M	M
Ge_2PAs	3.70	2.44	2.48	2.38	4.72	1.07	1.73	0.96	1.59
Ge_2PSb	3.84	2.60	2.47	2.44	4.84	M	0.55	M	0.37
Ge_2PBi	3.88	2.69	2.47	2.45	4.95	M	M	M	M

X atoms, resulting in a Janus structure. Following this replacement, Ge_2PX monolayer exhibits $P3m1$ space group with broken out-of-plane mirror symmetry compared to binary GeP counterpart, which has the space group of $P\bar{6}m2$. The 2D Janus structure consists of four atomic sublayers, forming a hexagonal primitive cell of the crystal. In this arrangement, two Ge atoms are located at the center, while X and P atoms occupy the top and bottom layers, respectively. The optimized lattice constants (a) for all Janus monolayers, along with their structural parameters including bond lengths for Ge-X, Ge-Ge, and Ge-P bonds ($d_{\text{Ge-}X}$, $d_{\text{Ge-Ge}}$, and $d_{\text{Ge-P}}$), as well as thickness (h), are illustrated in Fig. 1(c) and summarized in Table I. As one moves down the pnictogen group, the $d_{\text{Ge-}X}$ and $d_{\text{Ge-P}}$ bonds are elongated, leading to larger lattice constants. The calculated a and h values for Janus systems represent averages of those obtained in GeP and GeX monolayers [3]. Therefore, 2D Ge_2PX structures experience lattice strain on two atomic surfaces due to the modified lattice constants compared to their binary counterparts.

B. Dynamical stability

Following the structural optimization, the stability of the considered systems was assessed based on their phonon band dispersion relations, as presented in Fig. 2. The designed crystals were dynamically stable, with no imaginary frequencies observed throughout the BZ. As mentioned above, the primitive cell of Janus Ge_2PX monolayers consists of four atoms, each with three vibrational degrees of freedom resulting in twelve normal vibrational modes, three of which are acoustic with zero frequency at Γ point and nine are optical. In all of the 2D crystals, the flexural acoustic (ZA) branch exhibits a quadratic dispersion. In contrast, the transverse acoustic (TA) and the longitudinal acoustic (LA) branches show a linear dispersion near the zone center (Γ point) [48]. The highest frequency in the phonon band diagram ($\omega_{\max}$) in the given structures steadily decreases down the group of X atoms. This phenomenon arises from the increased atomic mass of the constituent atoms in the unit cell and the weakening of the interatomic force constants between these atoms. Additionally, phonon bands in the nanosheets become less dispersed across the entire frequency spectrum as the atomic weight of the pnictogen atoms increases. These less dispersive phonon bands may lead to higher scattering and, consequently, lower thermal conductivity. Furthermore, a gap is observed between
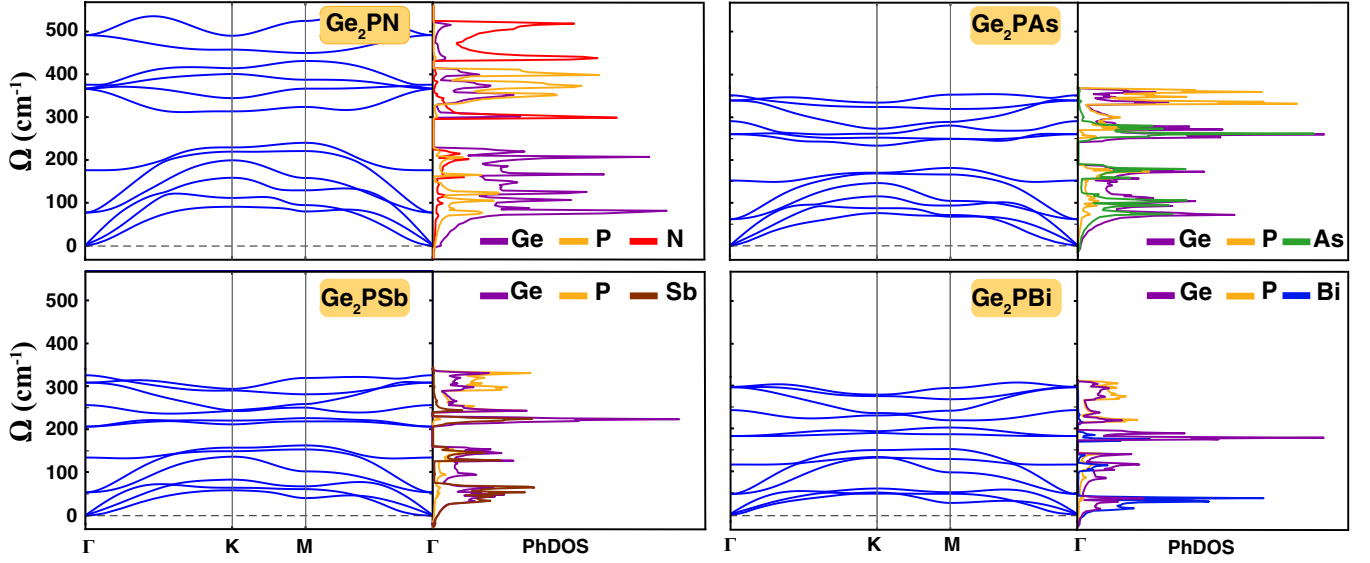
FIG. 2. Phonon dispersion diagrams for the Ge$_2$PX monolayers and the corresponding phonon density of states (PhDOS).

the higher and lower segments of the optical phonon modes in Ge$_2$PX monolayers. This phononic E_g arises from differences in binding strength and atomic mass among the constituent elements in the Ge$_2$PX Janus structures. The presence of a phononic E_g in a material restricts the propagation of mechanical waves at frequencies within the forbidden gap, making it a suitable candidate for vibrational insulating applications.

To interpret the phonon spectra of the proposed Janus structures, their corresponding phonon density of states (PhDOS) are presented in Fig. 2. PhDOS analysis reveals that the heavier elements in the nanosheets primarily contribute to the low-frequency vibrational modes, while the high-frequency phonon modes are characterized primarily by the lighter atoms in the crystals. Notably, in the Janus Ge$_2$PN monolayer, the highest optical vibrational modes originate from N atoms, whereas in other structures, they are determined by a combination of P and Ge atoms.

To further explore the dynamical stability of the designed systems, AIMD simulations were performed at elevated temperatures. In order to create proper conditions for any possible atomic rearrangements within the crystals and to remove constraints on the unit cell size, $4 \times 4 \times 1$ supercells were designed. Since the overall energy of the monolayers is sensitive to any bond reconstructions within the systems, the variation in gradient values of total energy as a function of simulation time is plotted to trace changes in their crystalline morphology. The fluctuation of the total energy of the systems with respect to simulation time, alongside snapshots of the atomic configuration at T = 300 K and 600 K, is illustrated in Fig. 3 and Fig. S1 within the Supplemental Material (SM) [49], respectively. According to the AIMD results, all the Janus structures maintain their atomic integrity without any considerable distortion up to 600 K, except for the Ge$_2$PBi monolayer, which retains its solidity up to 300 K. These findings manifest the dynamical stability of the Ge$_2$PX monolayers at elevated temperatures. At 600 K, none of the bonds between the constituent elements of Ge$_2$PN, Ge$_2$PAs,

and Ge$_2$PSb nanosheets are broken, while in the Ge$_2$PBi monolayer, Bi atoms are clearly detached from the system, indicating structural decomposition. The instability of the 2D Ge$_2$PBi structure is correlated with an asymmetric charge transfer from Ge to P and Bi atoms.

C. Vibrational properties

Raman spectroscopy is a conventional technique for the structural characterization of ultra-thin materials. The theoretical Raman spectrum serves as a useful tool for analyzing physical properties related to lattice symmetries, which, in turn, aids in the interpretation of experimental data. As mentioned above, the structural geometry of Ge$_2$PX monolayers belongs to the C$_{3v}$ symmetry group. The group theory analysis of phonon modes for the C$_{3v}$ space group at the zone center (Γ point) in Ge$_2$PX Janus structures can be expressed as $\Gamma_{\text{vib}}^{C_{3v}} = 4A_1 + 4E$.

This irreducible representation represents the total lattice vibration and comprises the terms for both acoustical and optical modes, as follows:

$$\Gamma_{\text{vib}}^{C_{3v}} = \Gamma_{\text{acoustic}} + \Gamma_{\text{optic}}, \Gamma_{\text{acoustic}} = A_1 + E, \Gamma_{\text{optic}} = 3A_1 + 3E,$$

where all E modes are represented as doubly degenerate in-plane vibrational modes, whereas all A$_1$ phonon modes are attributed to singly degenerate vibrations along the z direction. Acoustical modes consist of one A$_1$ and one E phonon mode, where all their frequencies at the Γ point are equal to zero. Moreover, the optical phonon modes are composed of three E and three A$_1$ vibrational modes. In a material or structure with C$_{3v}$ symmetry, the vibrational modes labeled as E and A$_1$ correspond to linear and quadratic functions of vibrational motion, respectively. As a consequence of their respective symmetrical behaviors, both E and A$_1$ modes are considered Raman active, meaning they can be detected using Raman spectroscopy. Thus, the Raman analysis of Ge$_2$PX Janus crystals should exhibit six peaks in their spectrum. For a further investigation of vibrational characteristics, Γ-centered
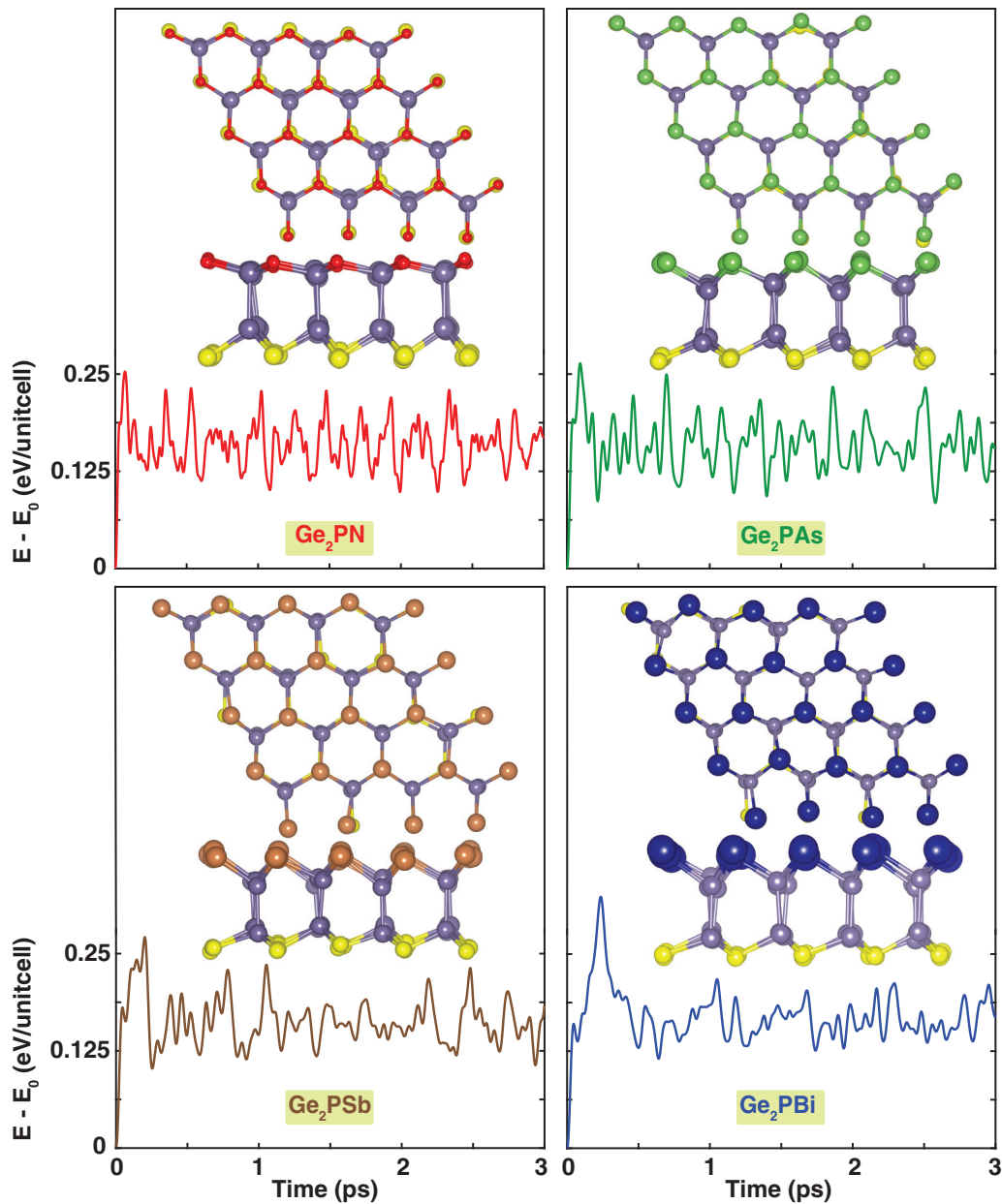
FIG. 3. The variation of the total energy of Janus Ge_2PX structures with the simulation time at T = 300 K. Final snapshots of atomic configurations at the end of *ab initio* molecular dynamics (AIMD) simulations are exhibited in the inset.

first-order off-resonant Raman spectra of the Janus nanosheets are computed and illustrated in Fig. 4(a). On each spectrum, the atomic displacements of the Raman-active modes are annotated to elucidate the origins of the Raman peaks. Our results indicate a clear correlation between the expansion of the atomic radius of the pnictogen atom (X) and a corresponding redshift in the Raman spectra. This phenomenon can be primarily attributed to the higher atomic mass and enhanced bonding strength within the material. In addition, in all Ge_2PX Janus monolayers, the third A_1 mode is very robust, mainly due to the higher contribution of the obtained out-of-plane macroscopic dielectric constants to the Raman tensors.

The vibrational vectors of the Raman-active modes for the Janus crystal are shown in Fig. 4(b). Due to the differing average atomic masses of GeP and GeX pairs, the correspond-

ing atomic displacements are not symmetric. In all Ge_2PX structures, the first optical mode is associated with the E representation, signifying a relatively low-frequency phonon mode arising from in-plane vibrations between GeP and GeX pairs. This initial double-degenerate mode is followed by the nondegenerate A_1 mode, which arises from the strong, opposing vibrations of GeP and GeX pairs along the out-of-plane direction. The second E vibrational mode is attributed to the vibrations of Ge and X atoms in the GeX pair, with the vibration of the GeP pair being negligible. An additional A_1 mode, located between two E phonon modes in the higher segment of the spectrum, represents the opposing out-of-plane vibration of Ge and X atoms in the GeX pair within the structures. In the third double-degenerate E mode, the vibration of the GeP pair predominantly contributes to the phonon
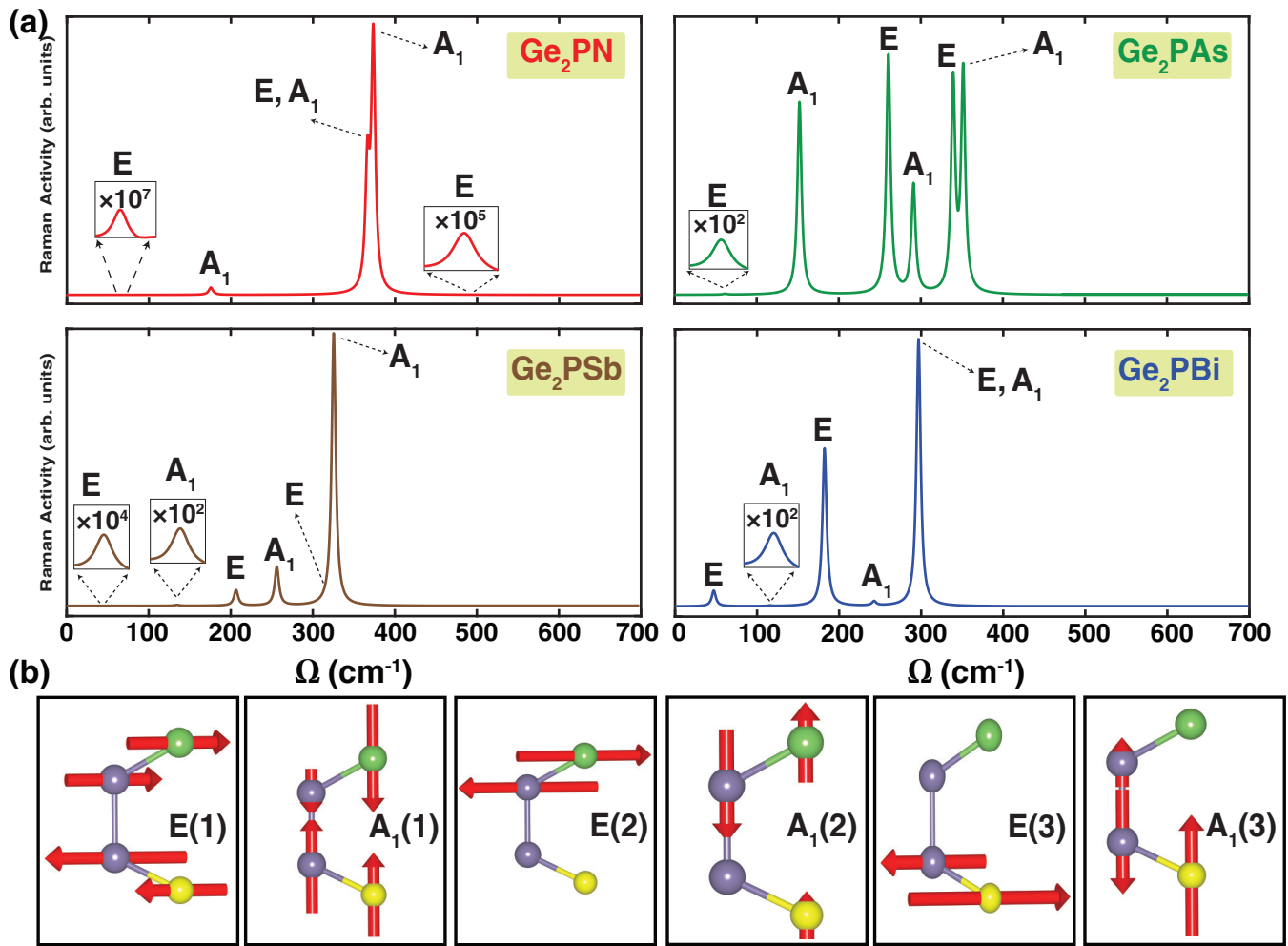
FIG. 4. (a) Raman spectra of the Ge_2PX monolayers and (b) the corresponding atomic displacements of the optical phonon modes in the structures.

mode, while Ge and P atoms vibrate in opposite in-plane directions. Lastly, the analysis of the third A_1 phonon mode reveals that the vibration of the GeP pair primarily contributes to the vibrational mode, with Ge and P atoms moving in opposite directions along the out-of-plane axis. It should be noted that there exists an inverse relationship between the activation energy of phonon modes and the mass of atoms in a crystal, as can be interpreted through the Debye model. In our case, the presence of heavier X atoms results in lower Debye temperatures and, consequently, lower activation energies for phonon modes. Notably, in the case of Ge_2PN, the highest optical mode is attributed to the E phonon mode, distinguishing it from other structures where the highest frequency at the Γ point is associated with the A_1 phonon mode. To model the eigenvector analysis of Ge_2PX Janus structures, we considered X as As, Sb, and Bi atoms. It is evident that for the Ge_2PN structure, the eigenvectors of GeP and GeX pairs should switch places.

D. Electronic properties

The electronic structure of Ge_2PX monolayers was investigated using the GGA-PBE and hybrid functionals, both with and without consideration of spin-orbit interactions. The

resulting E_g values are summarized in Table I, and the corresponding electronic band diagrams, including the effects of SOC, are shown in Fig. 5 for both GGA-PBE and HSE06 functionals. The electronic band structures calculated at the PBE level, along with PBE + SOC, indicate metallic behavior for all structures except the Ge_2PAs monolayer. However, HSE06 calculations reveal the semiconducting nature of the Ge_2PSb monolayer, correcting the underestimated E_g values. Due to the dissimilar dispersion characteristics of the electronic bands in different directions in BZ, Ge_2PX structures can be expected to exhibit anisotropic electronic properties. The valence band maximum (VBM) for these semiconductors is located at the Γ point, while the conduction band minimum (CBM) is found at the M point. A similar trend has been observed in the Janus Si_2XY (X, Y = P, As, Sb, and Bi) monolayers [29]. Based on the HSE06 calculations, incorporation of SOC reduces the E_g of the Ge_2PAs monolayer by 0.14 eV and the Ge_2PSb monolayer by 0.18 eV, with the SOC effect being more pronounced in materials containing heavier elements [50]. Moreover, with the exception of Ge_2PN, the (E_g) exhibits a narrowing trend down the group V, accompanied by an elongation of the Ge-X bond length (d_{Ge-X}). The large electronegativity difference between Ge and N,
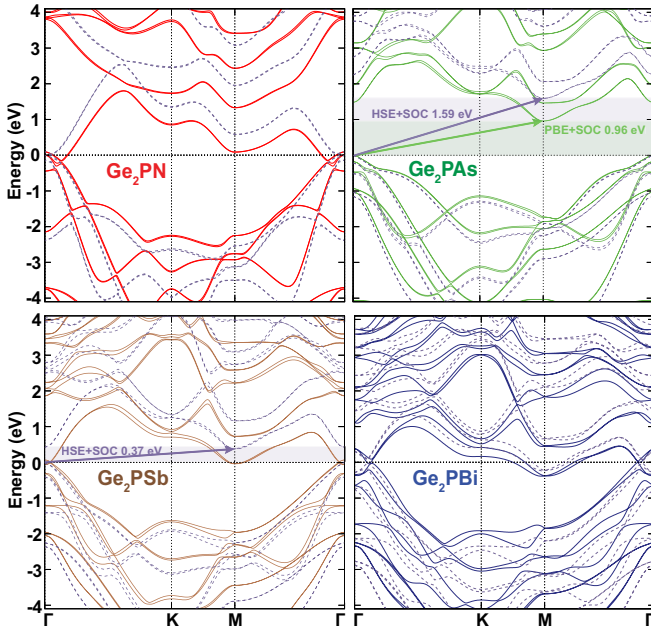
FIG. 5. The electronic band structures of the Janus Ge_2PX monolayers calculated within the level of PBE + SOC (solid lines) and HSE06 + SOC (dashed lines). The Fermi level is set to zero.

in comparison to Ge-P and Ge-X, leads to an asymmetric charge distribution in Ge_2PN, inducing out-of-plane polarization that profoundly influences bonding characteristics and results in a distinctive electronic response. This nonmonotonic behavior in E_g is also observed in other Janus monolayers [51,52]. Additionally, both Ge_2PAs and Ge_2PSb monolayers are subject to inherent lattice strain, resulting in reduced E_g values relative to their binary counterparts. For instance, the Ge_2PAs monolayer has a smaller E_g ($E_g^{HSE} = 1.73$ eV) than GeP ($E_g^{HSE} = 2.05$ eV) and GeAs ($E_g^{HSE} = 1.81$ eV) [3], which can be attributed to the stretching of the P side and the compression of the As side. The same applies to the Ge_2PSb configuration in comparison to its binary counterparts.

Ge_2PAs, with its indirect band gap of approximately 1.59 eV, exhibits promising characteristics for optoelectronic applications, particularly in light-emitting diodes (LEDs) and lasers [53]. This band gap aligns well with the energy requirements for emission in the visible or near-infrared range, positioning Ge_2PAs as a suitable candidate for devices operating within these wavelengths. On the other hand, Ge_2PSb, having a narrower E_g of about 0.37 eV, emerges as a material suitable for infrared optoelectronic applications. The lower E_g of Ge_2PSb is advantageous in scenarios such as telecommunications or night vision, where materials with lower E_g's are crucial for detecting and emitting infrared radiation [54]. Furthermore, the E_g of Ge_2PAs, exceeding 1.23 eV, presents opportunities for exploring photocatalytic applications, placing Ge_2PAs within a range generally considered suitable for such purposes [55]. The unique characteristics of Janus materials, particularly their out-of-plane polarization, position them as promising candidates for various piezoelectric applications, including sensors, actuators, and energy harvesting devices [30].

E. Thermoelectric properties

It is noteworthy that 2D systems possess the potential for enhanced thermoelectric (TE) performance compared to their 3D counterparts, attributed to the quantum confinement effect [56]. Both theoretical predictions and experimental demonstrations have revealed the improvements in the power factor (PF) and thermoelectric figure of merit (ZT) in various materials, including group III monochalcogenides, transition metal dichalcogenides, and tin chalcogenides [57–61], highlighting their potential for TE devices [62]. Despite many commercial 3D TE materials, such as Bi_2Te_3, typically exhibiting a ZT of around 1 near room temperature, experimental studies have shown that the Seebeck coefficient (S) of thin film WSe_2 can surpass that of Bi_2Te_3. Additionally, as the number of layers decreases, Bi_2Te_3 demonstrates higher ZT values, underscoring the effectiveness of the confinement effect in enhancing the TE efficiency of materials [63]. In this respect, we also examined the TE properties of Ge_2PX systems within the ballistic regime.

1. Phonon Thermal Transport

Within the framework of Landauer formalism, a comprehensive investigation of the phonon thermal transport properties of ternary Ge_2PX structures in the ballistic regime was conducted, providing valuable insights into their TE characteristics. Since no directional anisotropy was observed in electronic or phononic transmission spectra, results exclusively for only one direction were reported (see Figs. S2 and S3 within the SM [49]). As depicted in Fig. 2, all phonon frequencies exhibit a downward shift as the atomic weight of X increases along the group V. This shift results in a squeezing of the phonon bands, particularly the acoustic branches, into a narrower frequency range, leading to noticeable differences in the phonon transmission spectra [$\tau_{ph}(\omega)$] of the compounds as can be seen from Fig. 6(a). At low temperatures, the main contribution to the $\tau_{ph}(\omega)$ comes from acoustic modes. As proportional to the highest optical frequencies, $\tau_{ph}(\omega)$ of the lightest ternary Ge_2PN is spread out to higher frequencies, while at the heaviest Ge_2PBi the $\tau_{ph}(\omega)$ is suppressed to the lower frequencies. For comparison, $\tau_{ph}(\omega)$ of binary GeP is also calculated and its maximum value is indicated with a blue marker on the fourth panel in Fig. 6(a). Phonon thermal conductance (κ_{ph}) of Ge_2PX compounds was calculated as a function of temperature based on Eq. 4. κ_{ph} is obtained through a weighted integration spanning the entire frequency range of the phonon transmission function. The calculated κ_{ph} values per unit width are summarized in Table II for temperatures in the range 100–800 K. Notably, Ge_2PN exhibits the highest κ_{ph}, while Ge_2PBi shows a substantially lower κ_{ph} compared to the other compounds, consistent with their phonon transmission spectra. Additionally, the κ_{ph} value for binary GeP at 800 K is also included in Fig. 6(b) for reference.

While κ_{ph} exhibits a rapid increase at low temperatures, especially between 100 K and 200 K, it approaches convergence at different temperatures for each material. The convergence temperature is directly linked to the phonon weight factor, $\rho(\omega, T) = \hbar\omega(\partial f_{BE}(\omega, T)/\partial T)$, which governs the contributions of phonon modes to thermal conductance. $\rho(\omega, T)$ limits the contributions of high-frequency modes above the conver-
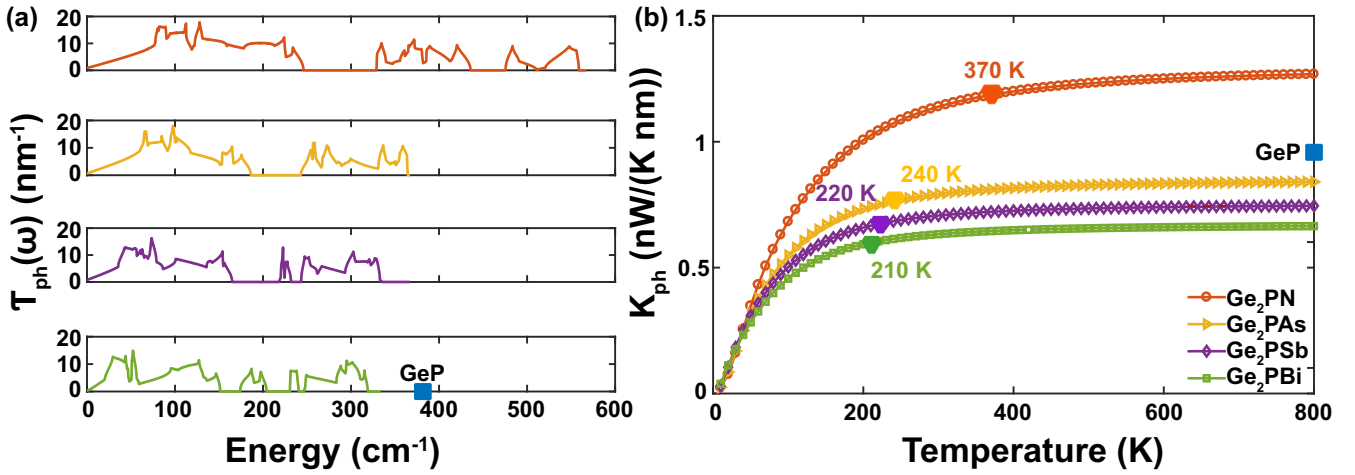
FIG. 6. (a) Phonon transmission spectra $[\tau_{ph}(\omega)]$ as a function of energy and (b) phonon thermal conductance (κ_{ph}) as a function of temperature for Ge$_2$PX monolayers. The blue squares indicates $\tau_{ph}(\omega)$ (maximum value) and κ_{ph} value of binary GeP at 800 K.

gence temperature values, allowing primarily low-frequency modes to participate in thermal transport. Herein, convergence temperature values for κ_{ph} of ternary structures have been determined as the temperature at which the $\rho(\omega)$ of each compound reaches a value of 0.99. In addition, when convergence temperature values are taken as reference, it is calculated that approximately 90% of the κ_{ph} values originate from contributions of acoustic and lowest energy optical phonon branches. Convergence temperature values of each κ_{ph} tend to increase as the atomic weight of the ternary compound decreases. The highest convergence temperature value of 370 K belongs to Ge$_2$PN, which is composed of the lightest species in the Ge$_2$PX family, while the heaviest compound, Ge$_2$PBi, reaches almost its maximum κ_{ph} at the lowest temperature of 210 K. Considering the κ_{ph} values, results unveil that the κ_{ph} values of semiconductor Ge$_2$PAs and Ge$_2$PSb are comparable to those InS from group III monochalcogenides, which is a promising p-type TE candidate at room temperature [64].

2. Electronic Transport and Thermoelectric Properties

It is a well-known fact that materials can exhibit a phenomenon called the bipolar effect when they lack a sufficient band gap relative to the operating temperature. This effect causes a drop in S at high temperatures for narrow-gap semiconductors, and for semimetals and metals, S can practically approach zero [65]. Considering this effect, hereafter we will

TABLE II. Phonon thermal conductance (κ_{ph}) per width values in a wide temperature range of 100–800 K.

GeX	κ_{ph} (nW/K/nm)			
	100 K	300 K	500 K	800 K
Ge$_2$PN	0.68	1.14	1.23	1.27
GeP	0.58	0.89	0.93	0.95
Ge$_2$PAs	0.55	0.79	0.83	0.84
Ge$_2$PSb	0.50	0.71	0.74	0.75
Ge$_2$PBi	0.46	0.63	0.66	0.67

focus our attention on studying the electronic transport and TE coefficients of the semiconductor Ge$_2$PAs and Ge$_2$PSb, as opposed to Ge$_2$PN and Ge$_2$PBi, which exhibit metallic character. To elucidate our theoretical findings, we need to examine electronic band structures of Janus Ge$_2$PAs and Ge$_2$PSb within the framework of transport concepts and compare them with binary GeP. In a prior study, the electronic properties of GeP have been explored employing HSE06 + SOC [3]. GeP exhibits a decent E_g value of 2.05 eV at the HSE06 level, which avoids the bipolar effect. In GeP, the topmost valence band (VB) takes on a Mexican hat shape (MHS), characterized by a quartic energy-momentum relation. This leads to a Van Hove singularity (VHS) in the density of states (DOS) near the VB edge. This step-like behavior in the transmission probability [$\tau(E)$] has been shown to enhance the S and, consequently, the thermoelectric figure of merit (ZT) in various previous theoretical studies [64,66–68]. Unlike the binary compound, Ge$_2$PAs and Ge$_2$PSb feature two adjacent parabolic VB that converge at the Γ point, resulting in orbital degeneracy. This degeneracy, in turn, increases the DOS effective mass (m_{DOS}^*), providing a considerable boost to the S [69] and TE efficiency. The MHS VB of Ge$_2$PAs and Ge$_2$PSb are positioned below the topmost degenerate parabolic VB, approximately 0.30 and 1.16 eV, respectively. The step-like $\tau(E)$ induced by the MHS bands are positioned at the same energy offsets (ΔE) away from the VB edge as shown in Fig. 7. Based on this band structure analysis, we can predict that the $\tau(E)$ of Ge$_2$PAs and Ge$_2$PSb is anticipated to reduce p-type S compared to binary GeP.

The L_n integrals given in Eq. (3) are critical in determining the electronic TE coefficients, and they rely on $\tau(E)$. In this respect, $\tau(E)$ for Ge$_2$PAs and Ge$_2$PSb were calculated with HSE06 functional with and without SOC and its variation is shown in Fig. 7. Note that $\tau(E)$ exhibits isotropic behavior, although dissimilar group velocities along different directions. In the case of Ge$_2$PAs, $\tau(E)$ changes gradually within the range from the VB edge to approximately 0.30 eV below it. Beyond this point, $\tau(E)$ starts to increase rapidly, primarily due to the involvement of the MHS band in the transport process. Interestingly, when SOC is considered, the
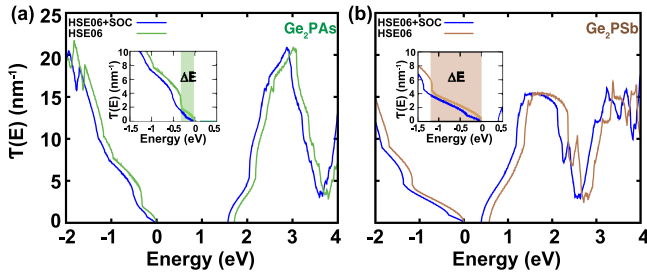
FIG. 7. The variation of electronic transmission spectra (obtained from band structure at the level of HSE06 with and without SOC) as a function of energy for Ge$_2$PAs and Ge$_2$PSb. The insets show the energy difference between contributions to $\tau(E)$ originated from parabolic and MHS bands.

rate of increase in $\tau(E)$ becomes even slower, and the step-like behavior of $\tau(E)$ undergoes some distortion. Moving on to Ge$_2$PSb, where the SOC effect is stronger due to the larger atomic weight, it is found that the energy dependence of $\tau(E)$ does not exhibit significant changes compared to that of Ge$_2$PAs. The influence of the SOC effect on the band gap and S will be discussed later on. With $\tau(E)$ determined for both structures, the TE can be calculated as functions of the chemical potential (μ) using the L_n integrals. The resulting electronic TE properties for both structures are presented in Figs. 8 and 9, covering the temperature range 100–800 K.

The electronic TE coefficients vary by both the energy dependence and the magnitude of $\tau(E)$. For example, S is interrelated with $\tau(E)$ through the Mott relation, $S(T, \mu) = -(\pi^2 k_B^2 T /3|e|)[\partial \ln \tau(E)/\partial E]$, a widely used formula for calculating S [70]. Although the relationship between S and $\tau(E)$ may not be explicitly apparent from the L_n integrals, it becomes evident when considering the Mott definition, which shows that the optimal S is achieved when there is a sharp change in $\tau(E)$ near the Fermi level. Indeed, the presence of a MHS topmost VB and the associated step-like $\tau(E)$ are more favorable for improving both S and PF.

The electrical conductance (G_e) as a function of μ for Ge$_2$PAs and Ge$_2$PSb is presented in terms of the quantum conductance unit ($G_0 = 2e^2/h$). While G_e reflects the smoothed behavior of $\tau(E)$ as the temperature increases, it precisely
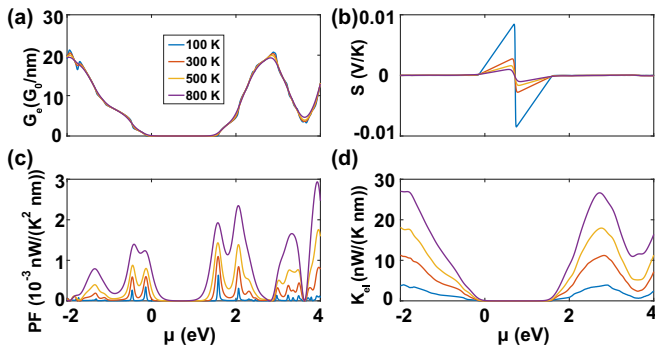

FIG. 8. Electronic TE coefficients for Ge$_2$PAs. (a) Electrical conductance G_e, (b) Seebeck coefficient S, (c) power factor PF, and (d) electrical thermal conductance κ_{el} as a function of chemical potential (μ).
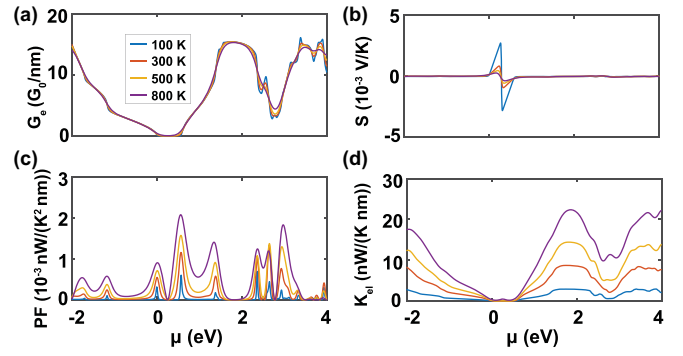

FIG. 9. Electronic TE coefficients for Ge$_2$PSb. (a) Electrical conductance G_e, (b) Seebeck coefficient S, (c) power factor PF, and (d) Electrical thermal conductance κ_{el} as a function of chemical potential (μ).

represents $\tau(E)$ at low temperatures (i.e., $T \rightarrow 0$). As μ increases, both G_e and κ_{el} exhibit an ascending trend for both structures, as observed in Figs. 8 and 9. Due to the smaller ΔE, p-type PF shows a "hump-shaped" character above 500 K for Ge$_2$PAs, which is advantageous for achieving high p-type ZT. Furthermore, Fig. 8 clearly illustrates that the n-type PF of Ge$_2$PAs attains higher values due to the less dispersive CB edge.

Due to the narrow band gap of Ge$_2$PSb, both minority and majority carriers simultaneously contribute to S, resulting in a reduction of S. In the case of Ge$_2$PSb, the bipolar effect becomes noticeable, especially after 600 K, further suppressing S. The inclusion of SOC reduces the band gap of Ge$_2$PSb from 0.55 to 0.37 eV, which strengthens the bipolar effect and significantly deteriorates S and consequently PF, especially after 400 K. Despite the expectation that the n-type PF of Ge$_2$PSb should be larger than that of Ge$_2$PAs due to the valley degeneracy at Γ and M points in the lowest conduction band, the first peak of the PF values is observed to be close for both structures. Similar to Ge$_2$PAs, Ge$_2$PSb does not exhibit a hump-shaped n-type PF and p-type PF due to the large ΔE.

ZT as a function of μ and temperature for Ge$_2$PAs and Ge$_2$PSb is illustrated in Figs. 10(a) and 10(b). Both structures exhibit nearly identical p-type ZT values up to 800 K. Ge$_2$PAs benefits from its quartic VB shape at high temperatures, attributed to the smaller ΔE, leading to enhanced p-type TE performance. However, when the SOC effect is considered, p-type ZT of Ge$_2$PAs decreases from 0.82 to 0.57 at 800 K. In contrast, Ge$_2$PSb, with its larger ΔE and low band gap, experiences a detrimental effect on its TE performance, despite its
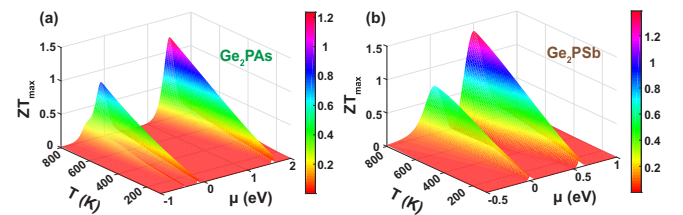

FIG. 10. Maximum ZT values as a function of temperature and chemical potential for (a) Ge$_2$PAs and (b) Ge$_2$PSb.

TABLE III. Peak *p*- and *n*-type *ZT* values in a wide temperature range of 100–800 K for GeP, Ge$_2$PAs, and Ge$_2$PSb.

	ZT (*p*/*n*)			
	100 K	300 K	500 K	800 K
GeP	0.31/0.05	0.69/0.22	1.10/0.76	1.72/1.71
Ge$_2$PAs	0.07/0.12	0.22/0.38	0.43/0.70	0.82/1.22
Ge$_2$PSb	0.07/0.13	0.22/0.44	0.43/0.83	0.72/1.38

lower κ_{ph}. The maximum *p*-type *ZT* achieved for Ge$_2$PSb is 0.72 at 800 K. This suggests that the low κ_{ph} counterbalances the losses arising from the large ΔE and low band gap. The inclusion of SOC leads to a significant decrease in *p*-type *ZT* from 0.72 to 0.29 due to changes in the energy dependence of $\tau(E)$. Both Ge$_2$PAs and Ge$_2$PSb showcase high *n*-type *ZT* values of 1.22 and 1.38 at 800 K, respectively. For comparison, TE coefficients and maximum *ZT* values of binary GeP are also calculated within the ballistic regime, as shown in Fig. S4 within the SM [49]. Binary GeP consistently possesses the highest *p*-type *ZT* values across all temperatures, mainly attributed to its topmost MHS VB (see Fig. S5 within the SM [49]). Specifically, GeP can achieve a maximum *ZT* as high as 1.72, approximately twice that of Ge$_2$PAs. However, GeP exhibits poor *n*-type *ZT* values up to 500 K compared to the Janus structures. The peak *p*- and *n*-type *ZT* values of GeP, Ge$_2$PAs, and Ge$_2$PSb are listed in Table III.

The TE efficiency of Ge$_2$PAs and Ge$_2$PSb can be improved through some approaches such as strain engineering. For instance, the MHS VB gives rise to VHS in the DOS at the VB edge. This singularity in DOS results in a step-like electronic transmission function, which leads to a high *S* and, consequently, a high *PF*, as previously reported. For Ge$_2$PAs, the parabolic and MHS VB coincide under 2% biaxial tensile strain, while the MHS band becomes the topmost VB at 6% strain in the case of Ge$_2$PSb as shown in Figs. S6 and S7 within the SM [49]. For Ge$_2$PAs, the absence of imaginary frequencies in its phonon spectrum ensures its dynamical stability. In contrast, Ge$_2$PSb does not maintain dynamical stability under 6% strain, as evident from its phonon dispersion (see Figs. S8 and S9 within the SM [49]). Therefore, we focus only on the TE properties of Ge$_2$PAs induced by biaxial tensile strain. A 2% biaxial tensile strain applied to Ge$_2$PAs led to the convergence of the valleys of both the MHS and parabolic VB, resulting in a step-like $\tau(E)$ as shown in Fig. S10 within the SM [49]. As mentioned earlier, the sharp increase in $\tau(E)$ enhances *S* and consequently *ZT*. The p_x and p_y orbitals of Ge, P, and As atoms contribute to the DOS of unstrained Ge$_2$PAs at the VB edge. Figure S11 within the SM [49] shows that VHS in DOS of Ge$_2$PAs arises from the p_z orbitals of elements and leads to an abrupt increase in transmission spectrum at the VB edge under 2% biaxial

tensile strain. Despite Ge$_2$PAs having a higher κ_{ph} compared to binary GeP, the peak *p*-type *ZT* value reached 1.6, as shown in Fig. S12 within the SM [49].

It is worth noting that the TE properties were investigated within the ballistic limit to provide insightful interpretations. However, extending calculations to a diffusive regime with the inclusion of the possible effects of quasi-particles [71,72], could provide a more comprehensive understanding for real-world applications [73].

IV. CONCLUSIONS

In conclusion, our systematic investigation of Janus Ge$_2$P*X* (*X* = N, As, Sb, Bi) monolayers has revealed promising TE performance and unique properties through comprehensive first-principles calculations. Our analysis of the phonon spectrum and high-temperature AIMD dynamics simulations has established the dynamical stability and structural integrity of these materials even at elevated temperatures. Furthermore, our study of vibrational analysis has identified distinct Raman-active modes for Ge$_2$P*X* monolayers, offering unique spectral signatures for these materials. Moreover, our HSE06 calculations, incorporating SOC interactions, have revealed that Ge$_2$PAs and Ge$_2$PSb monolayers exhibit anisotropic characteristics as indirect semiconductors in their electronic structure. This feature can enhance their potential for various electronic, and TE applications. Our investigation into thermal, electronic, and TE transport properties of Janus Ge$_2$P*X* monolayers, in comparison to binary GeP within the ballistic limit, has demonstrated that both Ge$_2$PAs and Ge$_2$PSb possess *n*-type *ZT* values exceeding 1 at 800 K. While binary GeP exhibits its highest *n*-type and *p*-type *ZT* values at high temperatures due to its Mexican hat shape (MHS) valence band, it is noteworthy that the *n*-type *ZT* values of Ge$_2$PAs and Ge$_2$PSb surpass those of GeP at room temperature. Additionally, our findings have demonstrated that the *n*-type *ZT* of Ge$_2$PAs can be significantly enhanced, reaching up to 1.6, through the application of biaxial tensile strain. Based on these results, our study positions Janus Ge$_2$P*X* monolayers as a promising area for further exploration and development in the field of energy harvesting and conversion. These materials hold great promise for advancing the efficiency of TE devices and contributing to sustainable energy solutions.

[1] M. N. Gjerding, A. Taghizadeh, A. Rasmussen, S. Ali, F. Bertoldo, T. Deilmann, N. R. Knøsgaard, M. Kruse, A. H. Larsen, S. Manti *et al.*, Recent progress of the computational 2D materials database (C2DB), 2D Mater. **8**, 044002 (2021).

[2] M. Ashton, S. B. Sinnott, and R. G. Hennig, Computational discovery and characterization of polymorphic two-dimensional IV-V materials, Appl. Phys. Lett. **109**, 192103 (2016).

[3] B. Özdamar, G. Özbal, M. N. Çınar, K. Sevim, G. Kurt, B. Kaya, and H. Sevinçli, Structural, vibrational, and electronic properties of single-layer hexagonal crystals of group IV and V elements, Phys. Rev. B **98**, 045431 (2018).

[4] T. Wadsten, Crystal structures of SiP$_2$, SiAs$_2$, and GeP, Acta Chem. Scand. **21**, 593 (1967).

[5] T. Wadsten, The crystal structure of SiAs, Acta Chem. Scand. **19**, 1232 (1965).

[6] C. Barreteau, B. Michon, C. Besnard, and E. Giannini, High-pressure melt growth and transport properties of SiP, SiAs, GeP, and GeAs 2D layered semiconductors, J. Cryst. Growth **443**, 75 (2016).

[7] F. Zhao, Y. Feng, and W. Feng, Germanium-based monoelemental and binary two-dimensional materials: Theoretical and experimental investigations and promising applications, InfoMat **4**, e12365 (2022).

[8] W. Zhang, J. Yin, Y. Ding, Y. Jiang, and P. Zhang, Strain-engineering tunable electron mobility of monolayer IV–V group compounds, Nanoscale **10**, 16750 (2018).

[9] W. Liu, S. Guo, G. Liu, X. Xia, Y. Huang, L. Xu, T. Guo, B. Cai, and S. Zhang, Electronic structure and quantum transport properties of 2D SiP: A first-principles study, J. Electron. Mater. **50**, 5499 (2021).

[10] F. Shojaei and H. S. Kang, Electronic structures and Li-diffusion properties of group IV-V layered materials: Hexagonal germanium phosphide and germanium arsenide, J. Phys. Chem. C **120**, 23842 (2016).

[11] A. Lou, Q.-B. Liu, and H.-H. Fu, Enhanced thermoelectric performance by lone-pair electrons and bond anharmonicity in the two-dimensional Ge$_2$Y$_2$ family of materials with Y = N, P, As, or Sb, Phys. Rev. B **105**, 075431 (2022).

[12] M. Yagmurcukardes, Y. Qin, S. Ozen, M. Sayyad, F. M. Peeters, S. Tongay, and H. Sahin, Quantum properties and applications of 2D Janus crystals and their superlattices, Appl. Phys. Rev. **7**, 011311 (2020).

[13] L. Zhang, Z. Yang, T. Gong, R. Pan, H. Wang, Z. Guo, H. Zhang, and X. Fu, Recent advances in emerging Janus two-dimensional materials: From fundamental physics to device applications, J. Mater. Chem. A **8**, 8813 (2020).

[14] J. Peng, Z.-j. Chen, B. Ding, and H.-M. Cheng, Recent advances for the synthesis and applications of 2-dimensional ternary layered materials, Research **6**, 0040 (2023).

[15] R. Li, Y. Cheng, and W. Huang, Recent progress of Janus 2D transition metal chalcogenides: From theory to experiments, Small **14**, 1802091 (2018).

[16] J. Zhang, S. Jia, I. Kholmanov, L. Dong, D. Er, W. Chen, H. Guo, Z. Jin, V. B. Shenoy, L. Shi et al., Janus monolayer transition-metal dichalcogenides, ACS Nano **11**, 8192 (2017).

[17] A.-Y. Lu, H. Zhu, J. Xiao, C.-P. Chuu, Y. Han, M.-H. Chiu, C.-C. Cheng, C.-W. Yang, K.-H. Wei, Y. Yang et al., Janus monolayers of transition metal dichalcogenides, Nat. Nanotechnol. **12**, 744 (2017).

[18] D. B. Trivedi, G. Turgut, Y. Qin, M. Y. Sayyad, D. Hajra, M. Howell, L. Liu, S. Yang, N. H. Patoary, H. Li et al., Room-temperature synthesis of 2D Janus crystals and their heterostructures, Adv. Mater. **32**, 2006320 (2020).

[19] Y.-C. Lin, C. Liu, Y. Yu, E. Zarkadoula, M. Yoon, A. A. Puretzky, L. Liang, X. Kong, Y. Gu, A. Strasser et al., Low energy implantation into transition-metal dichalcogenide monolayers to form Janus structures, ACS Nano **14**, 3896 (2020).

[20] R. Sant, M. Gay, A. Marty, S. Lisi, R. Harrabi, C. Vergnaud, M. T. Dau, X. Weng, J. Coraux, N. Gauthier et al., Synthesis of epitaxial monolayer Janus SPtSe, npj 2D Mater. Appl. **4**, 41 (2020).

[21] A. Kandemir and H. Sahin, Janus single layers of In$_2$SSe: A first-principles study, Phys. Rev. B **97**, 155410 (2018).

[22] H. D. Bui, H. R. Jappor, and N. N. Hieu, Tunable optical and electronic properties of Janus monolayers Ga$_2$SSe, Ga$_2$STe, and Ga$_2$SeTe as promising candidates for ultraviolet photodetectors applications, Superlattices Microstruct. **125**, 1 (2019).

[23] M. Demirtas, M. J. Varjovi, M. M. Cicek, and E. Durgun, Tuning structural and electronic properties of two-dimensional aluminum monochalcogenides: Prediction of Janus Al$_2$XX′ (X/X′: O, S, Se, Te) monolayers, Phys. Rev. Mater. **4**, 114003 (2020).

[24] Y. Ji, M. Yang, H. Lin, T. Hou, L. Wang, Y. Li, and S.-T. Lee, Janus structures of transition metal dichalcogenides as the heterojunction photocatalysts for water splitting, J. Phys. Chem. C **122**, 3123 (2018).

[25] R. da Silva, R. Barbosa, R. R. Mancano, N. Duraes, R. B. Pontes, R. Miwa, A. Fazzio, and J. E. Padilha, Metal chalcogenides Janus monolayers for efficient hydrogen generation by photocatalytic water splitting, ACS Appl. Nano Mater. **2**, 890 (2019).

[26] D. H. Ozbey, M. E. Kilic, and E. Durgun, Two-dimensional Janus GePAs monolayer: A direct-band-gap semiconductor with high and anisotropic mobility for efficient photocatalytic water splitting, Phys. Rev. Appl. **17**, 034043 (2022).

[27] M. Jakhar, A. Kumar, P. K. Ahluwalia, K. Tankeshwar, and R. Pandey, Engineering 2D materials for photocatalytic water-splitting from a theoretical perspective, Materials **15**, 2221 (2022).

[28] M.-Y. Liu, L. Gong, Y. He, and C. Cao, Intraband Lifshitz transition and Stoner ferromagnetism in Janus PA$_2$As (A = Si, Ge, Sn, and Pb) monolayers, Phys. Rev. B **104**, 035409 (2021).

[29] S. Babaee Touski and N. Ghobadi, Structural, electrical, and Rashba properties of monolayer Janus Si$_2$XY (X, Y = P, As, Sb, and Bi), Phys. Rev. B **103**, 165404 (2021).

[30] Y. Wu, C.-H. Yang, H.-N. Zhang, L.-H. Zhu, X.-Y. Wang, Y.-Q. Li, S.-Y. Zhu, and X.-C. Wang, The flexible Janus X$_2$PAs (X = Si, Ge and Sn) monolayers with in-plane and out-of-plane piezoelectricity, Appl. Surf. Sci. **589**, 152999 (2022).

[31] G. Kresse and J. Hafner, *Ab initio* molecular dynamics for liquid metals, Phys. Rev. B **47**, 558 (1993).

[32] G. Kresse and J. Hafner, *Ab initio* molecular-dynamics simulation of the liquid-metal–amorphous-semiconductor transition in germanium, Phys. Rev. B **49**, 14251 (1994).

[33] G. Kresse and J. Furthmüller, Efficiency of *ab-initio* total energy calculations for metals and semiconductors using a plane-wave basis set, Comput. Mater. Sci. **6**, 15 (1996).

[34] G. Kresse and J. Furthmüller, Efficient iterative schemes for *ab initio* total-energy calculations using a plane-wave basis set, Phys. Rev. B **54**, 11169 (1996).

[35] W. Kohn and L. J. Sham, Self-consistent equations including exchange and correlation effects, Phys. Rev. **140**, A1133 (1965).

[36] P. Hohenberg and W. Kohn, Inhomogeneous electron gas, Phys. Rev. **136**, B864 (1964).

[37] J. P. Perdew, K. Burke, and M. Ernzerhof, Generalized gradient approximation made simple, Phys. Rev. Lett. **77**, 3865 (1996).

[38] G. Kresse and D. Joubert, From ultrasoft pseudopotentials to the projector augmented-wave method, Phys. Rev. B **59**, 1758 (1999).

[39] P. E. Blöchl, Projector augmented-wave method, Phys. Rev. B **50**, 17953 (1994).

[40] H. J. Monkhorst and J. D. Pack, Special points for Brillouin-zone integrations, Phys. Rev. B **13**, 5188 (1976).

[41] S. Grimme, J. Antony, S. Ehrlich, and H. Krieg, A consistent and accurate *ab initio* parametrization of density functional dispersion correction (DFT-D) for the 94 elements H-Pu, J. Chem. Phys. **132**, 154104 (2010).

[42] S. Grimme, S. Ehrlich, and L. Goerigk, Effect of the damping function in dispersion corrected density functional theory, J. Comput. Chem. **32**, 1456 (2011).

[43] J. Heyd, G. E. Scuseria, and M. Ernzerhof, Hybrid functionals based on a screened Coulomb potential, J. Chem. Phys. **118**, 8207 (2003).

[44] J. Paier, M. Marsman, K. Hummer, G. Kresse, I. C. Gerber, and J. G. Ángyán, Screened hybrid density functionals applied to solids, J. Chem. Phys. **124**, 154709 (2006).

[45] A. Togo and I. Tanaka, First principles phonon calculations in materials science, Scr. Mater. **108**, 1 (2015).

[46] Y. Kruglyak, Landauer-Datta-Lundstrom generalized transport model for nanoelectronics, J. Nanosci. **2014**, 725420 (2014).

[47] K. Esfarjani, M. Zebarjadi, and Y. Kawazoe, Thermoelectric properties of a nanocontact made of two-capped single-wall carbon nanotubes calculated within the tight-binding approximation, Phys. Rev. B **73**, 085406 (2006).

[48] E. Mariani and F. von Oppen, Flexural phonons in free-standing graphene, Phys. Rev. Lett. **100**, 076801 (2008).

[49] See Supplemental Material at http://link.aps.org/supplemental/10.1103/PhysRevB.110.035411 for the variation of the total energy of Janus Ge_2PX structures with the simulation time at T = 600 K; direction dependent electronic and phonon transmission spectrum; electronic TE coefficients of binary GeP as a function of chemical potential; ZT_{max} as a function of temperature and chemical potential for binary GeP; electronic band structures, phonon dispersion diagrams, and PDOS of Ge_2PAs and Ge_2PSb under tensile strain; Seebeck coefficient S, power factor PF and thermoelectric figure of merit ZT of Ge_2PAs under tensile strain.

[50] J. Lee, W.-C. Tian, W.-L. Wang, and D.-X. Yao, Two-dimensional pnictogen honeycomb lattice: Structure, on-site spin-orbit coupling and spin polarization, Sci. Rep. **5**, 11512 (2015).

[51] X. Li, K. Zhang, X. Zeng, N. Li, and J. Wang, Electronic and photochemical properties of hybrid binary silicon and germanium derived janus monolayers, Phys. Chem. Chem. Phys. **23**, 17502 (2021).

[52] Z. Ma, T. Zhou, W. Duan, and Y. Huang, Recent progress in group-III metal chalcogenide based Janus materials: From properties to potential applications, J. Mater. Chem. C **11**, 16439 (2023).

[53] Z. Wang, Q. Jingjing, X. Wang, Z. Zhang, Y. Chen, X. Huang, and W. Huang, Two-dimensional light-emitting materials: Preparation, properties and applications, Chem. Soc. Rev. **47**, 6128 (2018).

[54] X. Wang, Y. Cui, T. Li, M. Lei, J. Li, and Z. Wei, Recent advances in the functional 2D photonic and optoelectronic devices, Adv. Opt. Mater. **7**, 1801274 (2019).

[55] S. Hu and M. Zhu, Ultrathin two-dimensional semiconductors for photocatalysis in energy and environment applications, ChemCatChem **11**, 6147 (2019).

[56] J. P. Heremans, M. S. Dresselhaus, L. E. Bell, and D. T. Morelli, When thermoelectrics reached the nanoscale, Nat. Nanotechnol. **8**, 471 (2013).

[57] N. T. Hung, A. R. Nugraha, and R. Saito, Two-dimensional InSe as a potential thermoelectric material, Appl. Phys. Lett. **111**, 092107 (2017).

[58] H. Ng, D. Chi, and K. Hippalgaonkar, Effect of dimensionality on thermoelectric powerfactor of molybdenum disulfide, J. Appl. Phys. **121**, 204303 (2017).

[59] J. Zeng, X. He, S.-J. Liang, E. Liu, Y. Sun, C. Pan, Y. Wang, T. Cao, X. Liu, C. Wang *et al.*, Experimental identification of critical condition for drastically enhancing thermoelectric power factor of two-dimensional layered materials, Nano Lett. **18**, 7538 (2018).

[60] Y. Zhao, P. Yu, G. Zhang, M. Sun, D. Chi, K. Hippalgaonkar, J. T. Thong, and J. Wu, Low-symmetry $PdSe_2$ for high performance thermoelectric applications, Adv. Funct. Mater. **30**, 2004896 (2020).

[61] M.-J. Lee, J.-H. Ahn, J. H. Sung, H. Heo, S. G. Jeon, W. Lee, J. Y. Song, K.-H. Hong, B. Choi, S.-H. Lee *et al.*, Thermoelectric materials by using two-dimensional materials with negative correlation between electrical and thermal conductivity, Nat. Commun. **7**, 12011 (2016).

[62] K. Kanahashi, J. Pu, and T. Takenobu, 2D materials for large-area flexible thermoelectric devices, Adv. Energy Mater. **10**, 1902842 (2020).

[63] G. Zhou and D. Wang, Few-quintuple Bi_2Te_3 nanofilms as potential thermoelectric materials, Sci. Rep. **5**, 8099 (2015).

[64] M. N. Çınar, G. Ö. Sargın, K. Sevim, B. Özdamar, G. Kurt, and H. Sevinçli, Ballistic thermoelectric transport properties of two-dimensional group III-VI monolayers, Phys. Rev. B **103**, 165422 (2021).

[65] Z. Dughaish, Lead telluride as a thermoelectric material for thermoelectric power generation, Phys. B: Condens. Matter **322**, 205 (2002).

[66] D. Wickramaratne, F. Zahid, and R. K. Lake, Electronic and thermoelectric properties of van der Waals materials with ring-shaped valence bands, J. Appl. Phys. **118**, 075101 (2015).

[67] C. Rudderham and J. Maassen, Analysis of simple scattering models on the thermoelectric performance of analytical electron dispersions, J. Appl. Phys. **127**, 065105 (2020).

[68] H. Sevinçli, Quartic dispersion, strong singularity, magnetic instability, and unique thermoelectric properties in two-dimensional hexagonal lattices of group-VA elements, Nano Lett. **17**, 2589 (2017).

[69] J. P. Heremans, V. Jovovic, E. S. Toberer, A. Saramat, K. Kurosaki, A. Charoenphakdee, S. Yamanaka, and G. J. Snyder, Enhancement of thermoelectric efficiency in PbTe by distortion of the electronic density of states, Science **321**, 554 (2008).

[70] M. Cutler and N. F. Mott, Observation of Anderson localization in an electron gas, Phys. Rev. **181**, 1336 (1969).

[71] W. H. Sio and F. Giustino, Polarons in two-dimensional atomic crystals, Nat. Phys. **19**, 629 (2023).

[72] N. Rivera, T. Christensen, and P. Narang, Phonon polaritonics in two-dimensional materials, Nano Lett. **19**, 2653 (2019).

[73] J. Wu, Y. Chen, J. Wu, and K. Hippalgaonkar, Perspectives on thermoelectricity in layered and 2D materials, Adv. Electron. Mater. **4**, 1800248 (2018).